interaction range, r_{AF}, as expected. These results are consistent with a short-range superexchange mechanism competing with a long-range kinetic-exchange mechanism.

Uniformly distributed ferromagnetically aligned Mn is thermodynamically more stable than all other configurations we have considered, with one exception: antiferromagnetic nearest-neighbor Mn dimers, for which the relative formation energy is −83 meV. This energy gain represents a driving force for reducing the amount of Mn available for ordering ferromagnetically. Thus, for a given total Mn concentration, the formation of AF Mn dimers will reduce the effective Mn concentration and T_c.

Finally, we address the predicted dependence of the Curie temperature on Mn concentration. At experimentally accessible concentrations, the average Mn-Mn separation is much larger than the FM interaction range, r_{FM}. This limits the applicability of mean-field theory for calculating the transition temperature, so we use a percolation approach (*27*), in which T_c is given by

$$k_B T_c = S(S + 1)J(R_{perc}), \qquad (2)$$

where k_B is the Boltzmann constant, S is the Mn spin (3/2), and R_{perc}, the radius of a ferromagnetically ordered Mn cluster at the percolation threshold, is proportional to the average Mn-Mn separation. Using the functional form in Eq. 1 for $J(r)$, we show in Fig. 4 (inset) the predicted dependence of the Curie temperature on Mn concentration for low concentrations (at higher concentrations, the short-range AF interactions become important, so that at its maximum near $x = 0.14$, the predicted T_c is only 50% higher than at $x = 0.035$). Although the behavior is qualitatively similar to that measured for the range of experimental compositions covered, the predicted temperatures are larger by roughly a factor of 4. This difference is due to three effects. First, the magnetization data indicate a magnetically active fraction of only 45 to 60%, which we attribute in part to the predicted formation of AF nearest-neighbor Mn dimers, effectively suppressing the measured Curie temperatures for a given concentration. The second effect is the well-known tendency of the LSDA to overestimate spin coupling strengths in antiferromagnetic insulators by factors ranging between 3 (*28*) and 6 (*29*); for kinetic exchange in a FM metal, this effect may be smaller but should still be present. The third effect is the absence of any hole compensation in our theory, which leads to theoretical hole densities of order 10^{22} cm^{-3}. This is far larger than the measured carrier concentrations ($\sim 10^{19}$ to 10^{20} cm^{-3}) and likely results in a further overestimate of the FM interaction strength. These considerations reconcile the difference between the experimental and predicted values and suggest avenues to improve our predictive ability in these complex materials.

References and Notes

1. C. Haas, *CRC Crit. Rev. Solid State Sci.* **1**, 47 (1970).
2. E. L. Nagaev, *Phys. Stat. Solidi B* **145**, 11 (1988).
3. H. Munekata *et al.*, *Phys. Rev. Lett.* **63**, 1849 (1989).
4. J. De Boeck *et al.*, *Appl. Phys. Lett.* **68**, 2744 (1996).
5. H. Ohno *et al.*, *Appl. Phys. Lett.* **69**, 363 (1996).
6. H. Ohno *et al.*, *Science* **281**, 951 (1998).
7. Y. Ohno *et al.*, *Nature* **402**, 790 (1999).
8. T. Hayashi *et al.*, *J. Appl. Phys.* **87**, 4673 (2000).
9. H. Ohno *et al.*, *Nature* **408**, 944 (2000).
10. G. A. Medvedkin *et al.*, *Jpn. J. Appl. Phys.* **39**, L949 (2000).
11. T. Dietl, H. Ohno, F. Matsukura, J. Cibert, D. Ferrand, *Science* **287**, 1019 (2000).
12. T. Dietl, H. Ohno, F. Matsukura, *Phys. Rev. B* **63**, 195205 (2001).
13. A discussion of the terminology can be found on *Science* Online at www.sciencemag.org/cgi/content/full/295/5555/651/DC1.
14. T. B. Massalaski, Ed., *Binary Alloy Phase Diagrams* (American Society for Metals, Metals Park, OH, ed. 2, 1990), vol. 2, p. 1964.
15. E. Abe, F. Matsukura, H. Yasuda, Y. Ohno, H. Ohno, *Physica E* **7**, 981 (2000).
16. Y. D. Park *et al.*, *Appl. Phys. Lett.* **78**, 2739 (2001).
17. H. Ohldag *et al.*, *Appl. Phys. Lett.* **76**, 2928 (2000).
18. A. Van Esch *et al.*, *Phys. Rev. B* **56**, 13103 (1996).
19. T. Omiya *et al.*, *Physica E* **7**, 976 (2000).
20. T. Maeda, H. Tanaka, *J. Cryst. Growth* **201–202**, 194 (1999).
21. F. Matsukura, H. Ohno, A. Shen, Y. Sugawara, *Phys. Rev. B* **57**, R2037 (1998).
22. Y. Iye *et al.*, *Mat. Sci. Eng. B* **63**, 88 (1999).
23. M. Fuchs, M. Scheffler, *Comput. Phys. Commun.* **119**, 67 (1999).
24. The ABINIT code is a common project of the Université Catholique de Louvain, Corning Incorporated, and other contributors (www.pcpm.ucl.ac.be/ABINIT).
25. T. C. Schulthess, W. H. Butler, *J. Appl. Phys.* **89**, 7021 (2001).
26. M. van Schilfgaarde, O. N. Mryasov, *Phys. Rev. B* **63**, 233205 (2001).
27. V. I. Litvinov, V. K. Dugaev, *Phys. Rev. Lett.* **86**, 5593 (2001).
28. J. Kortus, C. S. Hellberg, M. R. Pederson, *Phys. Rev. Lett.* **86**, 3400 (2001).
29. R. L. Martin, F. Illas, *Phys. Rev. Lett.* **79**, 1539 (1991).

30. This work was supported by the Office of Naval Research and the Defense Advanced Research Projects Agency Spins in Semiconductors program. Y.D.P., A.T.H., J.M.S., and T.F.A. are National Research Council Postdoctoral Associates. A.W. is an American Society for Engineering Education Postdoctoral Associate.

18 September 2001; accepted 21 December 2001

Nanocrystallization During Nanoindentation of a Bulk Amorphous Metal Alloy at Room Temperature

J.-J. Kim,[1] Y. Choi,[1] S. Suresh,[1]* A. S. Argon[2]

It is known that nanocrystallites can form in shear bands produced during severe bending or high-energy ball milling of thin ribbons of a metallic glass. We present direct experimental evidence that highly confined and controlled local contact at the ultrafine scale in the form of quasi-static nanoindentation of a bulk glassy metal alloy at room temperature can also cause nanocrystallization. Atomic force microscopy and transmission electron microscopy show that nanocrystallites nucleate in and around shear bands produced near indents and that they are the same as crystallites formed during annealing without deformation at 783 kelvin. Analogous to results from recent experiments with glassy polymers, our results are reasoned to be a consequence of flow dilatation inside the bands and of the attendant, radically enhanced, atomic diffusional mobility inside actively deforming shear bands.

The structure, thermodynamic stability, and electrical and magnetic properties of thin ribbons of amorphous metal alloys have been the focus of many theoretical and experimental investigations (*1–6*). With the development of techniques to produce bulk metallic glasses, the mechanical properties of amorphous alloys have also become topics of scientific and technological interest (*7–13*) in terms of structural and functional applications. Bulk amorphous alloys exhibit unique properties: high strength, localized deformation by shear banding, paucity of strain hardening, and much higher hardness than crystalline alloys of comparable elastic modulus. Because glassy alloys do not exist in thermodynamic equilibrium, they undergo crystallization with the supply of thermal energy.

Experiments have also shown that severe bending of thin ribbons of amorphous glasses can lead to the formation of shear bands within which nanocrystallites could be nucleated (*6*). In addition, high-energy ball milling or mechanical alloying of thin ribbons of some Al-based amorphous metals has been found to induce

[1]Department of Materials Science and Engineering, [2]Department of Mechanical Engineering, Massachusetts Institute of Technology, Cambridge, MA 02139–4307, USA.

*To whom correspondence should be addressed. E-mail: ssuresh@mit.edu

nanocrystallites whose underlying mechanistic processes can be different from those occurring during thermal anneal (*14*, *15*). Ball milling produces highly complex and uncontrolled stress states, and the possibility of substantial local heating during high-energy ball milling remains a topic of controversy. To our knowledge, no experimental information is currently available on the possibility of nanocrystallization in a bulk amorphous alloy subjected to well-controlled, slow (quasi-static), ultrafine-scale normal contact at room temperature. Such information would be of considerable use in elucidating the mechanisms of deformation-induced crystallization of an amorphous metal on several counts. (i) It is known that discontinuous shear bands form locally around indentations in bulk amorphous alloys (*12*, *13*). It would be of interest to ascertain whether nanocrystallites form in the vicinity of these indentation-induced bands. (ii) Nanoindentation provides a convenient and controlled method for introducing highly localized mechanical deformation into a bulk amorphous alloy at room temperature without the possibility of substantial increase in local temperature, which could alter microstructural evolution. (iii) Instrumented depth-sensing nanoindentation is becoming more widely used as a tool to extract the local mechanical properties of a broad range of materials, including amorphous alloys (*11*, *12*). It is of fundamental interest to learn whether and how microstructural changes can be introduced during nanoindentation; such changes, in turn, could influence the accuracy of mechanical property determination in glassy metal alloys.

The nominal chemical composition of the bulk metallic glass used in the present study was Zr-17.9Cu-14.6Ni-10Al-5Ti (atomic percent). The alloy was prepared by arc melting and the drop-casting method. The as-cast specimen was of cylindrical shape with a diameter of 6.7 mm, and the as-cast condition was verified to be fully amorphous. Further details on the melting and preparation of the alloy as well as basic structural evolution can be found in Liu *et al.* (*16*). Nanoindentation experiments were carried out on the alloy with a diamond Berkovich (three-sided pyramid) indenter mounted in a nanoindenter. Depth-sensing indentations covering a complete loading and unloading sequence were made, in a load-control mode, to maximum loads of 20 mN for the transmission electron microscope (TEM) and 20 mN and 60 mN for atomic force microscope (AFM) observations (*17*). The quasi-static indentation experiments were conducted at a loading/unloading rate of no more than 2 mN/s. Although nanoindentation of a bulk amorphous metal is a rather straightforward task, preparing TEM specimens containing the nanoindents (without inducing microstructural changes in the region surrounding the indent) and performing quantitative analyses of crystallization induced in and around the indents involve considerable experimental challenges. With these issues under consideration, we cut specimens of the metallic glass into the shape of a disc, 3 mm in diameter, and carefully thinned them to a thickness of 100 μm for later TEM observation. After indentation, we thinned the specimen only from the side opposite to the indented surface, and the time for dimpling was maximized to reduce the final ion-milling time. These precautions minimized any damage or change to the microstructure near the indented area. Subsequent foil preparation steps involved ion milling with the indented surface of the specimen facing down, and the ion-milling stage was shielded by a hollow metal cylinder to protect the indented side from redeposition of any sputtered species produced during the milling process. The TEM observations of the reference unindented regions also involved an identical ion-milling procedure so that the sole effects of nanoindentation on structural changes could be interpreted in a controlled manner.

Figure 1A shows an AFM image of discontinuous shear bands formed around an indent made under a maximum load of 60 mN (indenter penetration depth ~720 nm) in the glassy alloy. In this figure, the existence of intense bands of shear along the sides of the pyramidal impression bounded within the triangular indent is evident. Shear bands formed around an indent made at a maximum load of 20 mN (indenter penetration depth ~400 nm) are seen in the TEM image (Fig. 1B). Figure 2A is a dark-field TEM image of the center region of the indenter impression directly beneath the indenter tip. Also shown in this figure is the corresponding selected area diffraction (SAD) pattern. Because the aperture size for SAD is comparable to the indent size, electron diffraction produces both a diffused halo ring pattern, representative of the amorphous material, and distinct spots, representative of the nanocrystallites. Figure 2B is a dark-field TEM image of the indented region, where the dark triangular zone representing the indent impression is visible, because the surface thinned from the backside extended to the full depth of the indent. When the SAD pattern was obtained in a region located at a small distance from the indent, where no crystallites form, only a diffused ring pattern representing a fully amorphous material was observed (Fig. 2B, bottom right image). The same ring patterns associated with the fully amorphous structure were seen in the as-received material on which the same TEM foil preparation methods were used. On the other hand, SAD analysis of the indent reveals clear diffraction spots associated with the presence of nanocrystallites. The six spots, which are close to the exact Bragg condition, near the directly transmitted beam of the SAD pattern (Fig. 2B, bottom left image and schematic) were identified as being produced by diffraction from the (111) planes of Zr_2Ni nanoparticles. The presence of nanocrystallites can be clearly seen in the TEM image. It is also evident from the TEM images in Fig. 2, A and B, that the nanocrystallites form both along the faces of the indent and in the region beneath the indent tip, where the most severe deformation occurs. Analysis of the nanocrystallites indicates that the particles range in diameter from 10 to 40 nm, with a median particle diameter of approximately 20 nm. The surface uplift produced by the pileup of material around the indent is seen from the AFM image of Fig. 3A. Quantitative analysis of surface uplift in the AFM shows that indentation results in pileup as high as 150 nm above the average surface level in this nonhardening material (Fig. 3B), indicating the severity of local plastic flow around the indent.

Systematic experiments (*11*) on the crystallization of the present bulk amorphous alloy under thermal annealing, in the

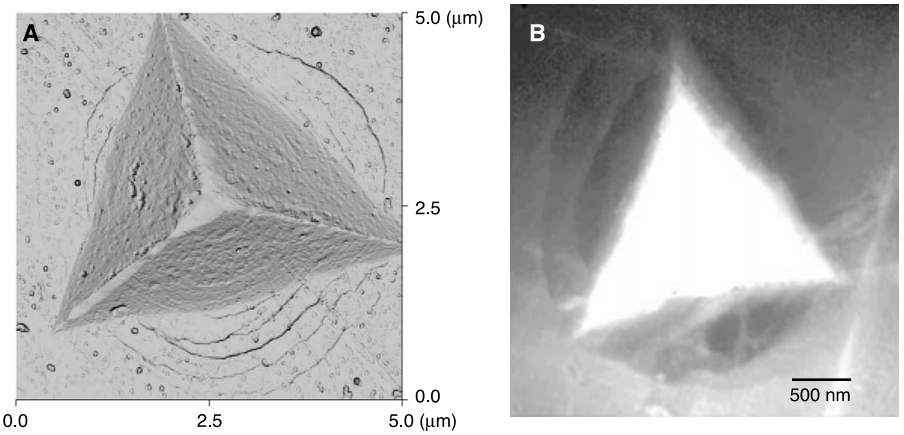

Fig. 1. Images of deformation around ultrafine-scale indents. (**A**) AFM illumination mode image (5 μm by 5 μm) of an indented impression after a 60-mN maximum load. The characteristic circular patterns around the triangular indent impression constitute pileup, which represents overlapping layers of displaced material. Similar patterns also can be found along the pyramidal faces of the indent. (**B**) Bright-field TEM image of an indented impression after a 20-mN maximum load. It also shows the same circular patterns around the triangular indent hole in a thin foil.

absence of any mechanical deformation, have shown that no discernible crystallization occurs up to a temperature of at least 683 K. At an annealing temperature of 783 K, partial crystallization occurs whereby primary crystallites of tetragonal Zr_2Ni nucleate. These crystallites are the same as those formed in the present nanoindentation experiments at room temperature. However, spot distributions in the SAD patterns of Fig. 2, A and B, show that the crystallographic orientations of nanocrystallites are not perfectly random. Preferential crystallographic alignment can occur in the deformation-induced nanocrystallites, unlike that seen during thermal annealing.

The formation of nanocrystallites in our nanoindentation tests, whose duration is roughly 10 s, points to the need for high atomic mobility. The rate-controlling process in the formation of Zr_2Ni is expected to be the diffusion of Ni. The required diffusion constant is simply estimated to be $D \sim L^2/4t$, where L is the distance over which the constituent atoms are gathered (which we estimate to be twice the average crystallite size of 20 nm), and $t = 10$ s is the indentation time. This gives $D \sim 4 \times 10^{-17}$ m^2/s. Diffusion constants of this magnitude are typically observed in metallic glasses only above their glass transition temperatures (T_g's) (*18*).

To explain such high atomic mobilities, several possibilities are considered here. Suggestions of local reordering during shear of an amorphous solid (*6*) have been made to explain the nucleation of stable clusters or embryos by exchange of atomic positions within shear bands during large deformation. However, no evidence has been provided, on the basis of such arguments, for the large atomic mobility needed to form crystallites that are 10 to 40 nm in size. A large rise in local temperature, of up to several hundred degrees, has also been suggested to result from the adiabatic shear of metallic glass (*19*). Such a situation, however, may be more likely during dynamic loading and/or fracture. For the present situation of shear bands connected to surrounding ideal heat sinks around quasi-statically produced indents, an estimate by Eshelby and Pratt (*20*) of temperature rise inside a shear band should be more appropriate.

$$\Delta T = \frac{\sigma \dot{\gamma}_b h}{2\pi k} \sqrt{\frac{\pi k \Delta\gamma}{c_p \dot{\gamma}_b}} \quad (1)$$

Here, σ (= 1.23 GPa) is the plastic shear (yield) resistance, $\dot{\gamma}_b$ is the shear strain rate inside the band, which is estimated to be 10^3 s^{-1} (*21*); h and $\Delta\gamma$ are the thickness and the total shear strain increment inside the band (which are estimated to be 12 nm and 2 nm, respectively, from Figs. 1A and 3); and k and c_p are the thermal conductivity and specific heat of the alloy, which should roughly equal 3.5 J m^{-1} s^{-1} K^{-1} and 5.5×10^6 J m^{-3} K^{-1} for a typical metallic glass (*16*, *22*). Evaluation of Eq. 1 gives a temperature rise of 0.05 K. Such estimates of negligible temperature rise are also consistent with experimental measurements of local temperature rise, even in the severely deformed plastic region of quasi-statically loaded crack tips (*23*). The influence of the hydrostatic pressure underneath the indenter on the crystallization temperature of the amorphous alloy strongly depends on composition and the density difference between the crystalline and amorphous phase. It is also known, however, that hydrostatic pressure markedly inhibits precipitate growth (*24*). In the present experiments, the nanocrystallites exhibit an average size of ~20 nm during quasi-static indentation experiments of only ~10 s in duration.

It has been proposed (*22*, *25*), and verified by direct measurements (*26*), that shearing of an amorphous material well below its T_g can result in flow dilatation, which autocatalytically causes intense shear localization within the shear bands themselves. More important, it has recently been established by direct diffusional measurements (*27*) that flow-induced dilatation inside actively deforming shear bands in disordered solids must have atomic-level topological features and mobility characteristics that are nearly identical to those at T_g of the solid, where thermally induced increase of local dilatation (free volume) results in a sharp reduction in interatomic interaction. Specifically, it has been shown that the penetration rate of a low-molecular-weight diluent into an actively plastically

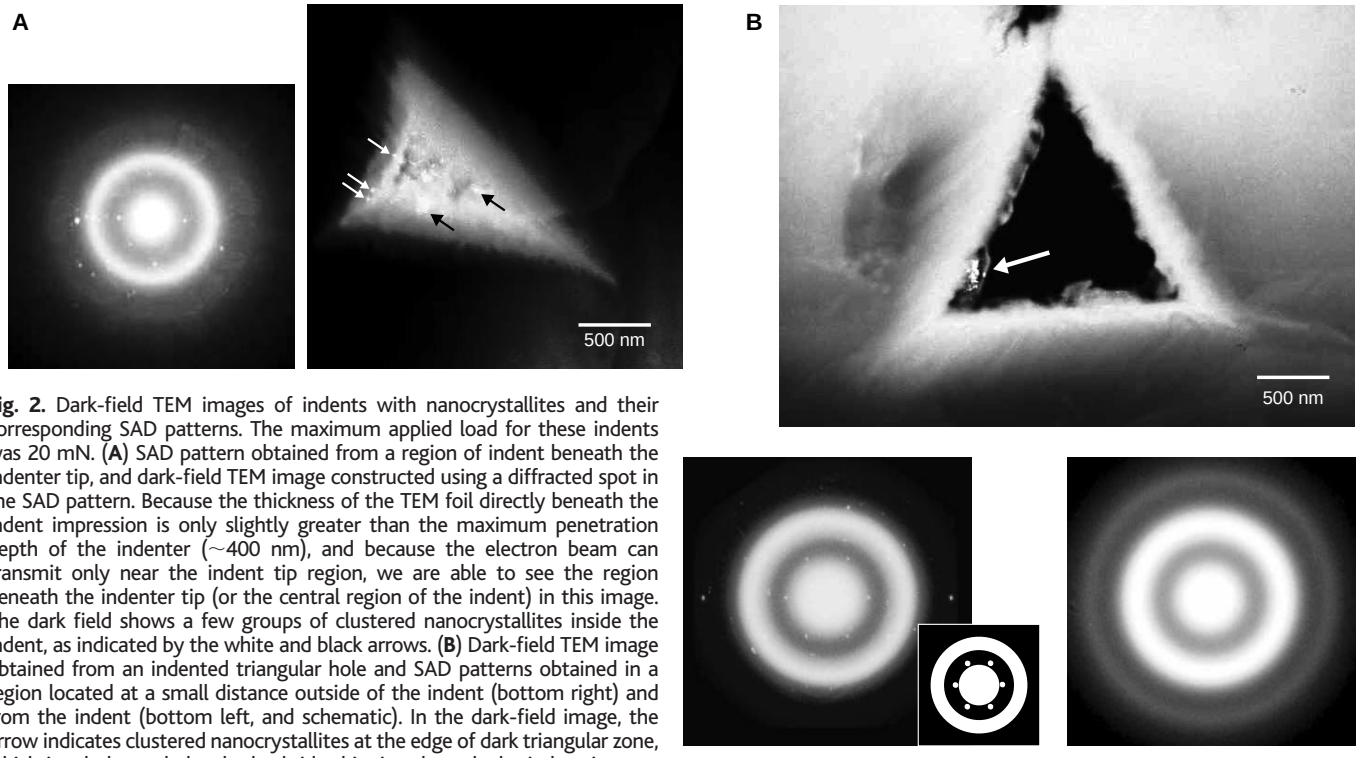

Fig. 2. Dark-field TEM images of indents with nanocrystallites and their corresponding SAD patterns. The maximum applied load for these indents was 20 mN. (**A**) SAD pattern obtained from a region of indent beneath the indenter tip, and dark-field TEM image constructed using a diffracted spot in the SAD pattern. Because the thickness of the TEM foil directly beneath the indent impression is only slightly greater than the maximum penetration depth of the indenter (~400 nm), and because the electron beam can transmit only near the indent tip region, we are able to see the region beneath the indenter tip (or the central region of the indent) in this image. The dark field shows a few groups of clustered nanocrystallites inside the indent, as indicated by the white and black arrows. (**B**) Dark-field TEM image obtained from an indented triangular hole and SAD patterns obtained in a region located at a small distance outside of the indent (bottom right) and from the indent (bottom left, and schematic). In the dark-field image, the arrow indicates clustered nanocrystallites at the edge of dark triangular zone, which is a hole made by the backside thinning through the indent impression. Six spots around the transmitted beam in the schematic, which are close to the exact Bragg condition, were analyzed and found to be associated with the (111) plane of tetragonal Zr_2Ni (space group *I4/mcm*, a = 6.49 Å, c = 5.28 Å). Halo rings of the bottom right SAD pattern without spots indicate the fully amorphous structure of metallic glass in a region that is not affected by the indentation.

deforming high-molecular-weight glassy polymer at 386 K is nearly identical to the penetration rate at the glass transition temperature of 486 K. Without active plastic flow, the penetration rate at 386 K is immeasurable, which indicates that the observed effect of plastic flow in this glass is equivalent to an increase in the diffusion constant by as much as a factor of 2×10^4 (*27*). Corresponding experiments in amorphous metals have not yet been performed, and there are important topological differences between glassy polymers and glassy metal alloys. However, there exists a striking similarity in the phenomenology and deformation mechanisms between the metallic and polymeric glasses (*28*). Therefore, we conclude that the observed rapid formation of Zr_2Ni nanocrystallites around the shear bands of our bulk amorphous alloy is a direct consequence of the inevitable dynamic flow dilatation in the actively deforming bands (without any substantial increase in temperature during plastic flow) and of the attendant dramatic enhancement in atomic diffusional mobility.

The present work provides direct experimental evidence that controlled and highly confined local contact deformation in the form of quasi-static nanoindentation of a bulk metallic glass at room temperature results in nanocrystallization. Additional features of the present experiments are that nanocrystallization due to ultrafine-scale contact occurs even without the possibility of substantial local heating and that the nanocrystallites are identified to be the same as those found during thermal anneal at 783 K without any mechanical deformation or indentation. To explain these results, we invoke a mechanistic rationale predicated on radically enhanced atomic diffusional mobility by drawing an analogy with recent experimental observations of enhanced diffusion in actively deforming amorphous polymers.

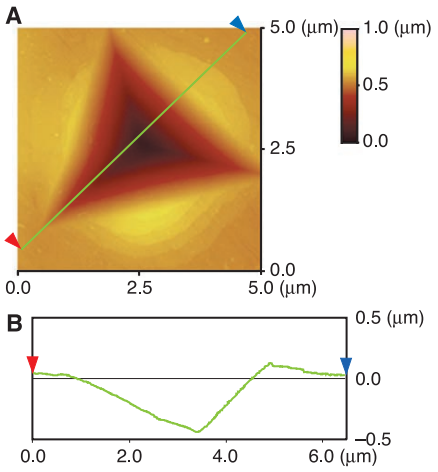

Fig. 3. AFM analysis after 60 mN of maximum load. (**A**) AFM height mode image (5 μm by 5 μm) of an indent. We also see the characteristic circular patterns around such an indent again, and the colored height information around the triangular indent reveals both large material pileup at the perimeter of the indent and overlapping layers of severely displaced materials. (**B**) Cross-sectional profile of the indent, along the green line of (A), showing the surface uplift along one side to be as high as 150 nm above the reference surface. This large pileup height around the perimeter of the indent, compared to the penetration depth (720 nm), indicates the severity of plastic flow around this region during indentation.

References and Notes

1. Y. He, S. J. Poon, G. J. Shiflet, *Science* **241**, 1640 (1988).
2. A. L. Greer, *Science* **267**, 1947 (1995).
3. I. Mat'ko, E. Illeková, P. Švec, P. Duhaj, *Mater. Sci. Eng.* **A225**, 145 (1997).
4. A. Makino, A. Inoue, T. Masumoto, *Mater. Trans. Jpn. Inst. Mater.* **36**, 924 (1995).
5. T. Masumoto, R. Maddin, *Mater. Sci. Eng.* **19**, 1 (1975).
6. H. Chen, Y. He, G. J. Shiflet, S. J. Poon, *Nature* **367**, 541 (1994).
7. A. Inoue, T. Zhang, T. Masumoto, *Mater. Trans. Jpn. Inst. Mater.* **31**, 177 (1990).
8. A. Peker, W. L. Johnson, *Appl. Phys. Lett.* **63**, 2342 (1993).
9. S. Suresh, Ed., *Acta Mater.* **48** (The Millennium Special Issue), 279 (2000).
10. P. E. Donovan, *Acta Metall.* **37**, 445 (1989).
11. J. G. Wang, B. W. Choi, T. G. Nieh, C. T. Liu, *J. Mater. Res.* **15**, 798 (2000).
12. R. Vaidyanathan, M. Dao, G. Ravichandran, S. Suresh, *Acta Mater.* **49**, 3781 (2001).
13. W. J. Wright, R. Saha, W. D. Nix, *Mater. Trans. Jpn. Inst. Mater.* **42**, 642 (2001).
14. Y. He, G. J. Shiflet, S. J. Poon, *Acta Metall. Mater.* **43**, 83 (1995).
15. K. Lu, *Mater. Sci. Eng.* **R16**, 161 (1996).
16. C. T. Liu *et al.*, *Metall. Mater. Trans. A* **29A**, 1811 (1998).
17. Nanoindentation experiments were conducted in a load-control mode with a NanoTest 600 (MicroMaterials, Wrentham, UK). For TEM observation, up to 400 indentations, equally spaced in the horizontal and the vertical directions with 20-μm separation, were made on the specimen that was previously cut into a disk 3 mm in diameter. For AFM, 10 indents for each load level were made. Electron microscopy studies were made using model 200CX, JEOL TEM (JEOL, Tokyo, Japan) operating at 200 kV. We prepared the specimens for TEM observations by ion-milling methods using a Gatan Duo-Mill (Gatan, Warrendale, PA) at 0.5 mA and 4 kV. The AFM studies were conducted on Nanoscope IIIa Scanning Probe Microscope from Digital Instruments.
18. B. Cantor, in *Amorphous Metals and Semiconductors*, P. Haasen, R. I. Jaffee, Eds. (Pergamon, Oxford, UK, 1986), pp. 108–125.
19. H. J. Leamy, H. S. Chen, T. T. Wang, *Metall. Trans.* **3**, 699 (1972).
20. J. D. Eshelby, P. L. Pratt, *Acta Metall.* **4**, 560 (1956).
21. H. Neuhauser, *Scr. Metall.* **12**, 471 (1978).
22. A. S. Argon, *Acta Metall.* **27**, 47 (1979).
23. K. M. Flores, R. H. Dauskardt, *J. Mater. Res.* **14**, 638 (1999).
24. W. H. Wang, D. W. He, D. Q. Zhao, T. S. Yao, M. He, *Appl. Phys. Lett.* **75**, 2770 (1999).
25. F. Spaepen, *Acta Metall.* **25**, 407 (1977).
26. J. Megusar, A. S. Argon, N. J. Grant, in *Rapidly Solidified Amorphous and Crystalline Solids*, B. H. Kear, B. C. Giessen, M. Cohen, Eds. (Elsevier, Amsterdam, Netherlands, 1982), pp. 283–287.
27. Q.-Y. Zhou, A. S. Argon, R. E. Cohen, *Polymer* **42**, 613 (2001).
28. A. S. Argon, in *Materials Science and Technology*, R. W. Cahn, P. Haasen, E. J. Kramer, Eds. (VCH, Weinheim, Germany, 1993), vol. 6, pp. 461–508.

29. Supported by the Defense University Research Initiative on NanoTechnology (DURINT) on "Damage- and Failure-Resistant Nanostructured and Interfacial Materials," funded at the Massachusetts Institute of Technology by the Office of Naval Research under grant N00014-01-1-0808. The authors are grateful to K. J. Van Vliet for valuable assistance with nanoindentation experiments, R. Vaidyanathan for helpful discussion, and C. T. Liu for providing the specimens. J.J.K. is grateful to the Center for Advanced Aerospace Materials at POSTECH, Pohang, Republic of Korea, for a postdoctoral fellowship.

28 September 2001; accepted 5 December 2001

Mineral Surface Control of Organic Carbon in Black Shale

Martin J. Kennedy,[1]* David R. Pevear,[1] Ronald J. Hill[2]

We show that 85% of variation in total organic carbon can be explained by mineral surface area in a black shale deposit from two locations in the late Cretaceous Western Interior Seaway, United States. This relation suggests that, as in modern marine sediments, adsorption of carbon compounds onto clay mineral surfaces played a fundamental role in the burial and preservation of organic carbon. Our data also provide evidence for organic matter within the smectite interlayer. This association implies that organic carbon sequestration in a representative oil-prone black shale facies may be more closely related to patterns of continental weathering and clay mineralogy than to ocean water chemistry or marine productivity.

The stratigraphic record is punctuated by intervals of organic carbon-rich sediments that form laterally persistent black marine shale and mudrock (*1, 2*). Many of these are important petroleum sources. It has been generally thought that organic matter (OM) in shale was deposited as discrete biogenic materials or particles, and the presence of these in shales has also been used to infer periods of ocean anoxia. Here we present evidence for an alternative model for the genesis of black shales, in which detrital smectite or smectitic mixed-layer illite-smectite (I-S)

[1]Department of Earth Science, University of California, Riverside, CA 92521, USA. [2]U.S. Geological Survey, Box 25045, Denver Federal Center, Mail Stop 939, Denver, CO 80225, USA.

*To whom correspondence should be addressed. E-mail: martink@mail.ucr